Available online at www.sciencedirect.com
SCIENCE DIRECT®
International Journal of Heat and Mass Transfer 48 (2005) 425–438
International Journal of HEAT and MASS TRANSFER
www.elsevier.com/locate/ijhmt

Quasi-static bubble formation on submerged orifices

D. Gerlach [a], G. Biswas [b,*], F. Durst [a], V. Kolobaric [a,1]

[a] Lehrstuhl für Strömungsmechanik, Universität Erlangen-Nürnberg, Cauerstr. 4, D-91058 Erlangen, Germany
[b] Department of Mechanical Engineering, Indian Institute of Technology, Kanpur 208016, India

Abstract

The static formation of air bubbles emanating from a submerged orifice was analyzed based on the principles of force balance. The analysis was corroborated by experiments using a shadow imaging technique. The influence of the Young contact angle of the three material components was investigated by identifying two modes of formation, corresponding to bubble formation at the orifice rim and spreading of the bubble base on the horizontal surface around the bubble. The characteristics of the formation process such as shape, height and volume of the bubble and the non-dimensional pressure difference at the orifice are given for both modes up to the critical equilibrium, defined by the maximum bubble volume, at which the bubble releases dynamically.

Keywords: Bubble formation; Submerged orifices; Aeration by bubbles

1. Introduction

Bubble formation at submerged orifices has widespread applications in various technological processes. Because the phenomena that occur are highly complex, attempts have been made to isolate some parameters systematically and to investigate them both analytically and experimentally. In the case of very small flow-rates and constant gas flow conditions, the formation takes place in a quasi-static manner and can thus be described by the Laplace equation as an equilibrium of surface, pressure and gravitational forces acting on the bubble surface [1,2]. The resulting ordinary differential equation can be solved numerically in such a way that complete sequences of bubble characteristics such as shape, volume, height and pressure variations at the orifice mouth are obtained up to the point of critical equilibrium, where the bubble reaches its maximum volume and will inevitably be released when further flow is added or if any small perturbation is applied [3,4].

Most of the work related to the bubble formation at submerged orifices require the bubble base to be fixed at the orifice rim [1,3–5], which is called mode A in the following. As an extension of this model, the influence of the wettability of the solid surface was investigated. This effect is characterized by the Young contact angle θ_0, which is the angle at equilibrium formed at the contact line of three phases on a horizontal and perfectly smooth surface [6]. In the present system the components are water, air and a solid surface, whereby the Young contact angle is measured from the horizontal plate through the liquid. It is known from Gibbs's inequalities [7], if a three-phase contact line coincides with an edge on a solid surface, the contact angle θ can take values of

* Corresponding author. Tel.: +91 512 597656; fax: +91 512 597408.
E-mail address: gtm@iitk.ac.in (G. Biswas).
[1] Present address: Institut für Strömungslehre und Wärmeübertragung, TU-Graz, Inffeldgasse 25/F, A-8010 Graz, Austria.

0017-9310/$ - see front matter © 2004 Elsevier Ltd. All rights reserved.
doi:10.1016/j.ijheatmasstransfer.2004.09.002

Nomenclature

a	Laplace constant (Eq. (6))
g	gravitational acceleration
h_0	submergence of the bubble apex
H	submergence of the orifice
K	orifice constant
P	pressure
P_σ	capillary pressure
P_0	ambient pressure
P_h	hydrostatic pressure
ΔP_s	non-dimensional pressure difference (Eq. (18))
Q	flow-rate through the orifice
r_b	radius of bubble base
r_s	orifice radius
R_0	radius of curvature at the apex of the bubble
R_1, R_2	radii of curvature
V	bubble volume
V_n	bubble volume above the bubble neck
x	radial coordinate component
y	axial coordinate component
y_s	bubble height

Greek symbols

β	shape factor (Eq. (8))
θ	instantaneous contact angle
θ_0	Young contact angle
θ_A	advancing contact angle
θ_R	receding contact angle
μ	dynamic viscosity
ρ	density
σ	surface tension

Subscripts

ch	chamber
crit	critical value
exp	experimental value
g	gas
l	liquid
max	maximal value
min	minimal value
s	quantity at the orifice
0	quantity at the apex of the bubble

Superscript

-	dimensional length

$\theta_0 \leqslant \theta \leqslant (180° - \phi) + \theta_0$, where ϕ is the angle of the solid wedge. This was derived theoretically by Dyson [8] and was proved experimentally by Mason and co-workers [9,10]. For the present case of a quasi-static bubble formation at a submerged orifice ($\phi = 90°$), this means that the instantaneous contact angle θ at the orifice rim will not fall below the Young contact angle θ_0 under static and ideal surface conditions. Instead, if θ reaches θ_0, the contact line will spread outward on the horizontal surface with $\theta = \theta_0$, called in the following mode B formation as in Ref. [11]. An exact analytical solution of the underlying ordinary differential equation of both modes exists only for very small bubbles or drops [11,12], i.e. near zero-gravity conditions, which is not valid for the orifice radii considered here.

Several theoretical investigations of the kind presented here exist for the case of a sessile or hanging drop. These studies on liquid drops apply the calculus of variations, whereby the change of the surface and potential energy due to small perturbations is considered, in order to find the characteristics at critical equilibrium, at which the volume of the drop reaches its maximal value and continues in an unstable and statically non-predictable manner [13–15]. Since these problems belong to the same family of analytical/numerical considerations as a submerged bubble forming in equilibrium, the available results of drop investigations were used for a correct theoretical description of the present work.

Comparisons between the solutions of the Laplace equation and experiments can be found for hanging drops [16] and external interfaces to a circular cylinders [17]. Longuet-Higgins et al. [4] confirmed their theoretically calculated shapes of a bubble formed at the rim of an orifice (mode A) by comparing the bubble height. A fairly close agreement was obtained. Very recently Gnyloskurenko et al. [18] performed an experimental study on the influence of wetting conditions on the bubble formation under quasi-static conditions. With help of recorded pictures they described the development of the parameters of interest. The theory of contact angle hysteresis was used to explain the results. Unlike this investigation the authors have chosen a different approach. A model was developed to compute complete formation processes following modes A and B by solving the Laplace equation under given boundary conditions, in which the bubble base is allowed to spread over the surrounding plate. This method provides us with an exact knowledge of the characteristics during the quasi-static formation under ideal conditions. Under such conditions the surface is perfectly smooth and no surface inhomogeneities are present, i.e. no contact angle hysteresis is occurring. To verify the predicted bubble shapes

for the two modes a projection method (shadow imaging) was applied. The measurements were made under static conditions for three orifice radii (0.5, 1 and 2 mm) and two orifice materials (brass and Teflon). The characteristics at bubble departure obtained theoretically were found to differ significantly between the two modes of formation. This demonstrates the importance of the plate material employed in combination with the fluids, which has not received considerable attention up to now. Some disagreement between theoretical and experimental results arose for the case of mode B formation owing to the imperfect surface condition always present in experiments, but the present results were found to be consistent with the theory of contact angle hysteresis of moving contact lines [19].

This paper is arranged as follows. Starting from the force balance at a point of the interface of a static bubble, a non-dimensional ordinary differential equation is derived and numerical solutions are obtained for different boundary conditions. The experimental approach of shadow imaging is described in Section 2. The results are introduced by a discussion about the parameters pertaining to the present quasi-static case. Subsequently the theoretical results are demonstrated and compared with the experimental data obtained for the modes A and B bubble formation. Finally, conclusions are drawn.

2. Theoretical prediction of the bubble profile

Let us consider the configuration of a bubble growing on a small, submerged orifice. The origin of the coordinate system is placed in this case at the vertex with a $\bar{y}$-coordinate pointing downwards in the direction of the gravitational force, as indicated in Fig. 1. While considering the quasi-static formation of the bubble, the effect of the flow through the orifice on the pressure variations and the influence of the viscous stresses are assumed to be negligible small. The remaining forces acting on an interfacial element are the gas pressure P_g, the capillary pressure P_σ, the ambient pressure P_0 and the hydrostatic pressure P_h. The resultant pressure balance is

$$P_g = P_\sigma + P_0 + P_h = \left(\frac{1}{\overline{R}_1} + \frac{1}{\overline{R}_2}\right)\sigma + P_0 + \rho_l g(\bar{h}_0 + \bar{y}), \tag{1}$$

where $\overline{R}_1$ and $\overline{R}_2$ are the radii of curvature of the interface at the point $(\bar{x}, \bar{y})$, σ is the (constant) surface tension, ρ is the density of either the liquid or gas (subscript l or g), g is the acceleration due to gravity and the bar denotes that all the marked quantities express dimensional lengths. The bubble pressure can be written as

$$P_g = P_{g,0} + \rho_g g\bar{y} = \frac{2\sigma}{\overline{R}_0} + P_0 + \rho_l g\bar{h}_0 + \rho_l g\bar{y}, \tag{2}$$

where $P_{g,0}$ is the bubble pressure at the vertex, where the radius of curvature of the bubble apex is $\overline{R}_1 = \overline{R}_2 = \overline{R}_0$. Introducing Eq. (2) into (1), we obtain

$$\frac{2\sigma}{\overline{R}_0} = \left(\frac{1}{\overline{R}_1} + \frac{1}{\overline{R}_2}\right)\sigma + (\rho_l - \rho_g)g\bar{y}. \tag{3}$$

For the solution of Eq. (3) we apply the following relations for the radii of curvature:

$$\overline{R}_1 = \frac{(1+\bar{y}'^2)^{3/2}}{\bar{y}''}, \qquad \overline{R}_2 = \frac{\bar{x}(1+\bar{y}'^2)^{1/2}}{\bar{y}'}, \tag{4}$$

where primes indicate the derivative with respect to $\bar{x}$, yielding an ordinary differential equation as follows

$$\frac{\bar{y}''}{(1+\bar{y}'^2)^{3/2}} + \frac{\bar{y}'}{\bar{x}(1+\bar{y}'^2)^{1/2}} = \frac{2}{\overline{R}_0} - \frac{2\bar{y}}{a^2}, \tag{5}$$

where

$$a^2 = \frac{2\sigma}{(\rho_l - \rho_g)g} \tag{6}$$

is the Laplace constant. By normalizing Eq. (5) with respect to a, i.e. $x = \bar{x}/a$, $y = \bar{y}/a$ and $R_0 = \overline{R}_0/a$, we obtain the following non-dimensional form:

$$\frac{y''}{(1+y'^2)^{3/2}} + \frac{y'}{x(1+y'^2)^{1/2}} = \frac{2}{R_0} - 2y. \tag{7}$$

For static bubble formation as considered in this paper, no closed-form solution appears to exist for this ordinary differential equation in which the radius of curvature at the vertex remains as a parameter. Only for the case of very small bubbles or drops, where the conditions are near to zero-gravity conditions, Chesters [12] found an analytical solution of Eq. (7). This solution can be assumed to be a good approximation, if the 'shape factor' β obeys

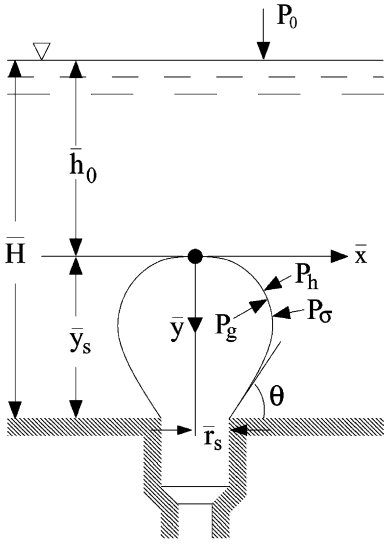

Fig. 1. Choice of coordinate system and balance of forces.

$$\beta = \frac{(\rho_l - \rho_g) g \overline{R}_0}{\sigma} \leqslant 0.1. \tag{8}$$

To provide a numerical solution, Eq. (7) can be reduced to two first-order equations by substitution of

$$z = \frac{y'}{(1+y'^2)^{1/2}} \tag{9}$$

according to Lohnstein [20]. This results in the following first-order differential equations:

$$\frac{dz}{dx} = -\frac{z}{x} + 2\left(\frac{1}{R_0} - y\right), \tag{10}$$

$$\frac{dy}{dx} = \frac{z}{(1-z^2)^{1/2}}, \tag{11}$$

which can be integrated with the initial conditions

$$y = 0 \quad \text{and} \quad z = 0 \quad \text{at } x = 0.$$

Care has to be taken when $dy/dx \approx 1$, because this represents an inflection point of the computed bubble shape. After reaching $dy/dx = 1$, the dependent variable is changed by substituting $u = (1 - z^2)^{1/2}$. From there onwards, we solve for x by advancing y with help of the following equations:

$$\frac{du}{dy} = \frac{(1-u^2)^{1/2}}{x} - 2\left(\frac{1}{R_0} - y\right), \tag{12}$$

$$\frac{dx}{dy} = \frac{u}{(1-u^2)^{1/2}}. \tag{13}$$

The final values of the solution of Eqs. (10) and (11), say y_1 and x_1, are used as the initial conditions for solving Eqs. (12) and (13).

Based on the solution of Eqs. (10)–(13), the non-dimensional bubble volume V can be determined by partial integration:

$$V = \pi \int_0^y x^2 \, dy = \pi x^2 y - 2\pi \int_0^x xy \, dx. \tag{14}$$

Eq. (10) can be written as $d(xz)/dx = 2x(1/R_0 - y)$, which allows us to calculate Eq. (14) as

$$V = \pi x \left[z + x\left(y - \frac{1}{R_0} \right) \right]. \tag{15}$$

The non-dimensional pressure variation can be obtained in the following way [1]. The pressure at the apex can be written as

$$P_{g,0} = \frac{2\sigma}{\overline{R}_0} + P_0 + \rho_l g(\overline{H} - \bar{y}_s). \tag{16}$$

This can be introduced into Eq. (2) to obtain the pressure at the orifice as follows

$$P_{g,s} = \frac{2\sigma}{\overline{R}_0} + P_0 + \rho_l g \overline{H} - g(\rho_l - \rho_g)\bar{y}_s. \tag{17}$$

The non-dimensional pressure difference at the orifice is then

$$\Delta P_s = \frac{1}{\sqrt{2\sigma g(\rho_l - \rho_g)}} (P_{g,s} - P_0 - \rho_l g \overline{H}) = \frac{1}{R_0} - y_s. \tag{18}$$

3. Experimental study: shadow imaging

In the present investigation, attempts were made to validate the theoretical predictions of static bubble formation on submerged orifice experimentally. For measurements of the bubble contour, we applied a shadow image method in which an "imperfect" diffuser, as recommended by Lunde and Perkins [21], was placed at the opposite side of a CCD camera. For the actual investigation, the orifice was placed in a container and submerged 15 cm below the free water surface. The bubble growing on the orifice produced a sharp shadow in the far field which was recorded by the CCD camera. An infusion pump was used together with a gas-tight glass syringe (10 ml) to provide a constant flow-rate through the orifice. The infusion pump controlled the inflow rate through the orifice in the range 9×10^{-4} ml/min $< Q <$ 20 ml/min with less than 0.1% error. The syringe was equipped with a capillary of length 5 cm and inner diameter 0.8 mm. The orifice (Fig. 2) was connected to the thin capillary of the air supplying syringe to reduce the influence of the chamber volume on the formation process [1,5]. Orifice radii of 0.5, 1 and 2 mm are considered in the present experiments. In order to verify the theoretical predictions of modes A and B, i.e. the formation at the orifice rim and the spreading of the bubble base, orifice plates made of brass and Teflon were used. According to the Young contact angle (θ_0), measured from the liquid side of the contact line, Teflon ($\theta_0 = 108°$, [6]) in combination with water and air is well documented as a non-wetting ($\theta_0 > 90°$) material under ideal conditions, in contrast to wetting materials with ($\theta_0 < 90°$). As shown in the subsequent section, high values of θ_0 can force the bubble base to spread over the plate surface (mode B), so that the Teflon plates were lapped to yield nearly smooth surfaces for mode B

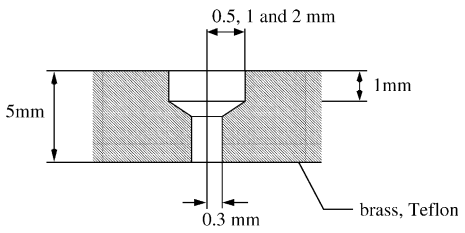

Fig. 2. Orifice geometry.

experiments. In contrast, if the bubble base remains at the orifice rim (mode A), θ_0 has no influence of the formation process. Hence, for the validation of the bubble shapes forming during mode A formation, brass plates were used, which were not subject of special surface treatments.

Demineralized water was used in all experiments in order to minimize the effect of liquid contamination on the bubble formation process. The large cross-section of the water tank (100×100 mm) relative to the size of the bubbles ensured that the influence of the tank walls was negligible small.

For capturing the shape of the bubble at various stages of the formation process, an 80c60 HiSense CCD camera was used equipped with 1280×1024 light sensitive cells. We employed a field of view of typically 23.5×18.8 mm with a spatial resolution of about 1.8×10^{-5} m/pixel.

In order to extract the bubble outline from the intensity image obtained by the CCD camera, the following image processing method was applied. From the intensity histogram the intensity threshold was carefully determined to convert the gray-scale image into a binary image. The outline of the bubble was then preserved by means of an edge detection algorithm. Hence a closed contour of the bubble, i.e. of the entire bubble shape, was obtained by an 8-connected sequence of pixels (typically 300–1000 coordinate points depending on the size of the bubble).

4. Results and discussion

Attempts were made to improve upon the basic knowledge of the physics of bubble formation on upward-facing orifices. The authors' own investigations and publications in the literature show that the entire topic appears to be very complex. Clift et al. [5] listed the following influencing parameters on the bubble volume for a perfectly wetted orifice:

$$V_{\text{bubble}} = f(Q, \bar{r}_s, \rho_l, \mu_l, \sigma, \rho_g, \mu_g, K, V_{ch}, g, \overline{H}), \tag{19}$$

where Q is the time-mean flow-rate, K is an orifice constant, V_{ch} is the chamber volume below the orifice and $\bar{r}_s$, ρ_l, μ_l, ρ_g, μ_g, σ, g and $\overline{H}$ are the orifice radius, density and viscosity of the liquid and the gas, respectively, the surface tension, the gravitational acceleration and the submergence as defined in Section 2. Simplifications can be made, taking into consideration the effect due to the chamber volume and the connection between the orifice and chamber. If the chamber volume is very large compared with the bubble volume formed, the pressure in the chamber is not influenced significantly by the varying flow-rate through the orifice, and this case is thus called the constant pressure case. The other limiting case for the bubble formation on orifices is the constant flow regime, whereby the pressure drop between orifice and chamber is higher than the pressure variations in the bubble.

By applying the experimental setup described in Section 3, conditions of a constant flow regime could be produced. The use of the syringe pump allowed the flow-rate Q to be accurately decreased to very small values. Typically the flow-rate was set to 0.01 ml/min, which resulted in bubble formation times of several minutes. This clearly justifies the assumption of quasi-static bubble formation. Comparisons of bubble shapes from experiments with different flow-rates ($0.005 \leqslant Q \leqslant 5$ ml/min) and the corresponding data from numerical computations showed that under such conditions the bubble volume after departure was independent of the flow-rate through the orifice. An increase in Q caused an increase in the bubble frequency, as also stated in the literature [5].

Taking the above considerations into account, Eq. (19) can be simplified by omitting the parameters Q, μ_l, μ_g, V_{ch} and K. The ordinary differential Eq. (5), which describes the shape of a bubble in equilibrium, has no dependence on the submergence H. Hence we also cancel H, which leaves us with the following expression:

$$V_{\text{bubble}} = f(\bar{r}_s, \rho_l, \sigma, \rho_g, g). \tag{20}$$

ρ_g can easily be included in the theoretical treatment in Section 2 and thus remains, despite $\rho_g \ll \rho_l$ for water and air. Considering Eq. (20), it comes out that the volume of the static bubble formed at the rim of an orifice can be characterized by $r_s = \bar{r}_s/a = \bar{r}_s/\sqrt{2\sigma/(\rho_l - \rho_g)g}$, whereby the Laplace constant results from Eq. (5) to be the unit length for normalization.

Since the parameters given in Eq. (19) are only valid for a perfectly wetted orifice, a further parameter has to be incorporated, which takes the wettability of the orifice into account. The bubble forms at the rim of the orifice if the instantaneous contact angle θ (see Fig. 1) during bubble formation is larger than the Young contact angle θ_0, which is defined by the equilibrium of the contact line between gas, liquid and solid. Otherwise, if θ becomes θ_0, the bubble base spreads out, keeping the contact angle constant as $\theta = \theta_0$ [7–11]. These two modes are denoted below modes A and B according to Chesters [11]. Accurate knowledge about these two modes are necessary, since, as will be shown, the maximal static bubble volume can differ significantly between the two modes. Furthermore, the Young contact angle is very sensitive to the ambient conditions such as roughness of the plate and liquid contamination by surface-active substances. Hence modes A and B are examined theoretically based on the analytical solution and compared with the experimental results obtained under quasi-static conditions.

4.1. Mode A bubble formation

In order to investigate bubble formation under quasi-static conditions theoretically, Eqs. (10)–(13) were solved employing a fourth-order Runge–Kutta scheme. For a given orifice radius r_s a sequence of bubble shapes can be found by varying the parameter R_0 (radius of curvature at the apex). The numerical calculations were started with $R_0 \to \infty$, the bubble volume $V = 0$ and the height of the apex $y_s = 0$, i.e. a horizontal free air/water interface. To proceed with the computations R_0 was decreased in small steps and the computations searched for a new bubble shape with a slightly increased volume and height. The increase in bubble volume from step to step in the calculations was restricted to a small value in the present implementation, since more than one solution exists if r_s and R_0 are fixed [13]. Those additional solutions turn out to be unstable and thus can be reached in experiments only transiently [4]. In order to avoid a jump in the bubble volume V, the apex radius R_0 and the bubble height y_s, the computations only allowed changes of V and R_0 to be extremely small. It was also required that the height of the bubble y_s increased successively with volume, which was shown by Pitts [15] theoretically to result in the stable formation of bubbles exposed to all physically possible perturbations. Following this procedure, the computations resulted in a sequence of bubble characteristics, which describe the stable stages of a bubble formed at an underwater orifice. For each orifice radius, the computations finally reached a point where no further solution according to the above restrictions could be found. The volume of the bubble at this critical equilibrium corresponded to the maximal volume [3,13], denoted V_{max}. At this final stage any perturbation, e.g. a continuation of the flow through the orifice, leads inevitably to the release of the bubble.

The accuracy of the numerical approach was validated by recalculation of the results of Longuet-Higgins et al. [4], who used a solution process following Pitts [14] and therefore different to the present one. For example, for an orifice radius $r_s = 0.35355$ (corresponding to the case of a diameter $D = 1$ normalized with the unit of length of $(\sigma/\rho g)^{1/2}$ used in Ref. [4]) our results agree with their data for the values at critical equilibrium R_0 and V_{max} within the accuracy of the third decimal place given in [4].

The results obtained in the authors' computation are shown in Figs. 3 and 4. The quantities x, y, R_0 and V are all normalized with the Laplace constant a (=3.858 mm for water and air at ambient temperature; see Eq. (6)), the non-dimensional pressure difference is defined in Eq. (18) and the instantaneous contact angle θ at the bubble base is given by

$$\frac{dy}{dr} = \tan(\theta), \tag{21}$$

and needs, together with Eq. (11), no further explanation.

To explain static bubble formation further it is worth noting that the bubble formation starts with a flat surface defined by $R_0 \to \infty$, $y_s = 0$ and $\theta = 180°$. During the initial stage R_0 decreases and the pressure difference at the orifice mouth increases with volume. If the orifice radius is smaller than a critical value of $r_{s,crit} = 0.6343$ (e.g., [4]), the parameter R_0 will pass through a minimum, as can be seen in Fig. 3(b), e.g., at $r_s = r_{s,crit}$ the tangent at the point of inflection of the profiles becomes vertical.

The results presented here both theoretically and experimentally focus on $r_s < r_{s,crit}$. Detailed examinations of Figs. 3(b) and 4 show that the minimum in R_0 and θ and the maximum in the pressure difference are not located at the same volume V for constant r_s. It

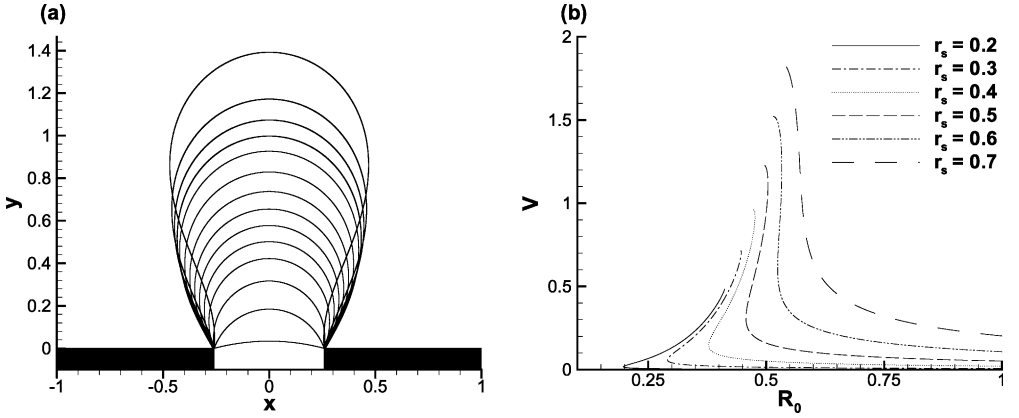

Fig. 3. Development of the bubble shape for $r_s = 0.259$ ($\bar{r}_s = 1$ mm, (a)) and the parameter R_0 for different orifice radii (b). x, y, R_0 and V are normalized with the Laplace constant a (see Eq. (6)).

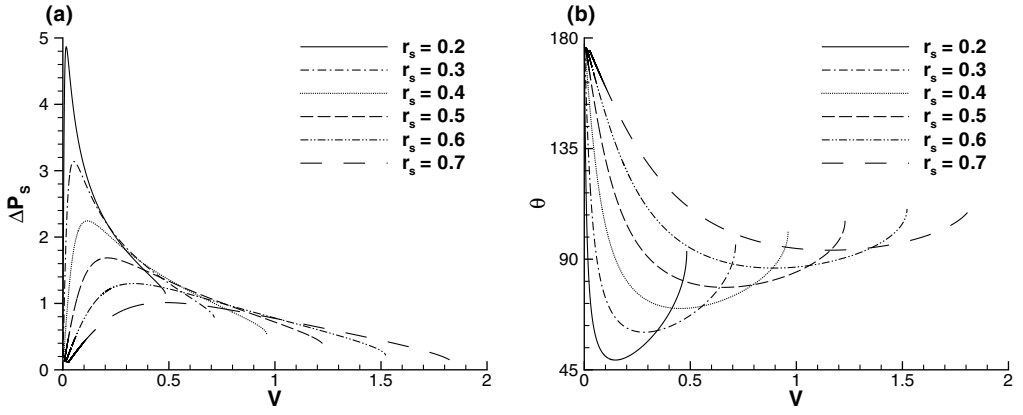

Fig. 4. Development of the non-dimensional pressure difference ΔP_s at the orifice (a) and the instantaneous contact angle θ at the bubble base (b) for different orifice radii.

can clearly be seen that the characteristics of small r_s show strong variations during static bubble formation, which can be ascribed to the predominant role of surface tension for small bubbles. In contrast, R_0 stays approximately constant for large values of r_s (Fig. 3(b)). Since the results in this section are concerned with mode A of bubble formation, the bubble base is fixed at the orifice edge. If the instantaneous contact angle θ falls below the Young contact angle, the bubble base begins to spread (mode B). As shown in Fig. 4(b) small orifice radii favor spreading of the bubble base, since smaller values of θ are reached during formation. Further discussions about mode B are presented in the next section.

Using the experimental setup described in Section 3, the authors were able to provide constant flow conditions and the bubbles could be produced in a quasi-static manner. Orifice plates made of brass were used to obtain bubble formation processes following mode A. Fig. 5(a)–(d) compare the predicted and the experimentally obtained bubble shapes for different stages of growth for the case of $r_s = 0.259$. The agreement is indeed excellent. (All experimental results of bubble contours are shown by their pixel coordinates, which appear in the figures as a solid line.) The corresponding theoretical contour was determined by fixing r_s, y_s and the area confined by the contour. Since the calculation of the axisymmetric bubble volume based on the experimental data would require an interpolation of the pixel coordinates, the quality of the contours was verified by comparing the area instead. Differences in area smaller than 1.5% confirm the accuracy of the experimental approach. For convenience, each stage of formation shown is marked in an R_0–y_s plot (Fig. 5(e)). Additionally, Fig. 6 gives an impression of the static bubble growth at the larger orifice radius investigated ($r_s = 0.518$, $\bar{r}_s = 2$ mm). The smallest orifice radius ($r_s = 0.130$) was found to spread outwards (mode B). This is in agreement with the predictions given above that small orifices facilitate the bubble base to spread, since smaller values of θ are obtained during formation (Fig. 4(b)).

Table 1 summarizes the results obtained from the computations ($V_{\max}, R_{0,\max}, y_{s,\max}, V_n, \theta_{\min}$) and the experiments ($y_{s,\exp}$) related to mode A formation of bubbles. Here $V_{\max}$ is the maximal volume at critical equilibrium, $R_{0,\max}$ and $y_{s,\max}$ are the corresponding radius of curvature and the height of the apex, V_n is the gas volume above the neck at the critical equilibrium and $\theta_{\min}$ is the smallest instantaneous contact angle obtained for constant r_s. V_n is assumed to describe the total volume of a released bubble more precisely since it cannot be expected that the complete air mass above the orifice detaches. In general, V_n is smaller than V and only exists for $r_s < r_{s,\text{crit}}$. Additionally, $y_{s,\max}$ is compared between theory and experiment for the three cases considered ($\bar{r}_s = 0.5$, 1 and 2 mm). The smallest orifice ($r_s = 0.130$) is found to result in bubble release following mode B, which is due to fact that small orifices reach smaller values of θ at the bubble base (see Fig. 4(b)). Results of mode B formation are provided in the following section. The maximal heights of $y_{s,\max}$ in the two remaining cases ($r_s = 0.259$ and 0.518) are 8.6% and 8.4% lower than the predicted value. This can be explained by the experimental uncertainties and the small vibrations always present in experimental measurements.

4.2. Mode B bubble formation

Similarly to the previous section, mode B bubble formation will be discussed first from the theoretical point of view and then it will be compared with the experiments undertaken. Instead of fixing the bubble base to a specific value (mode A), we permitted in a second set

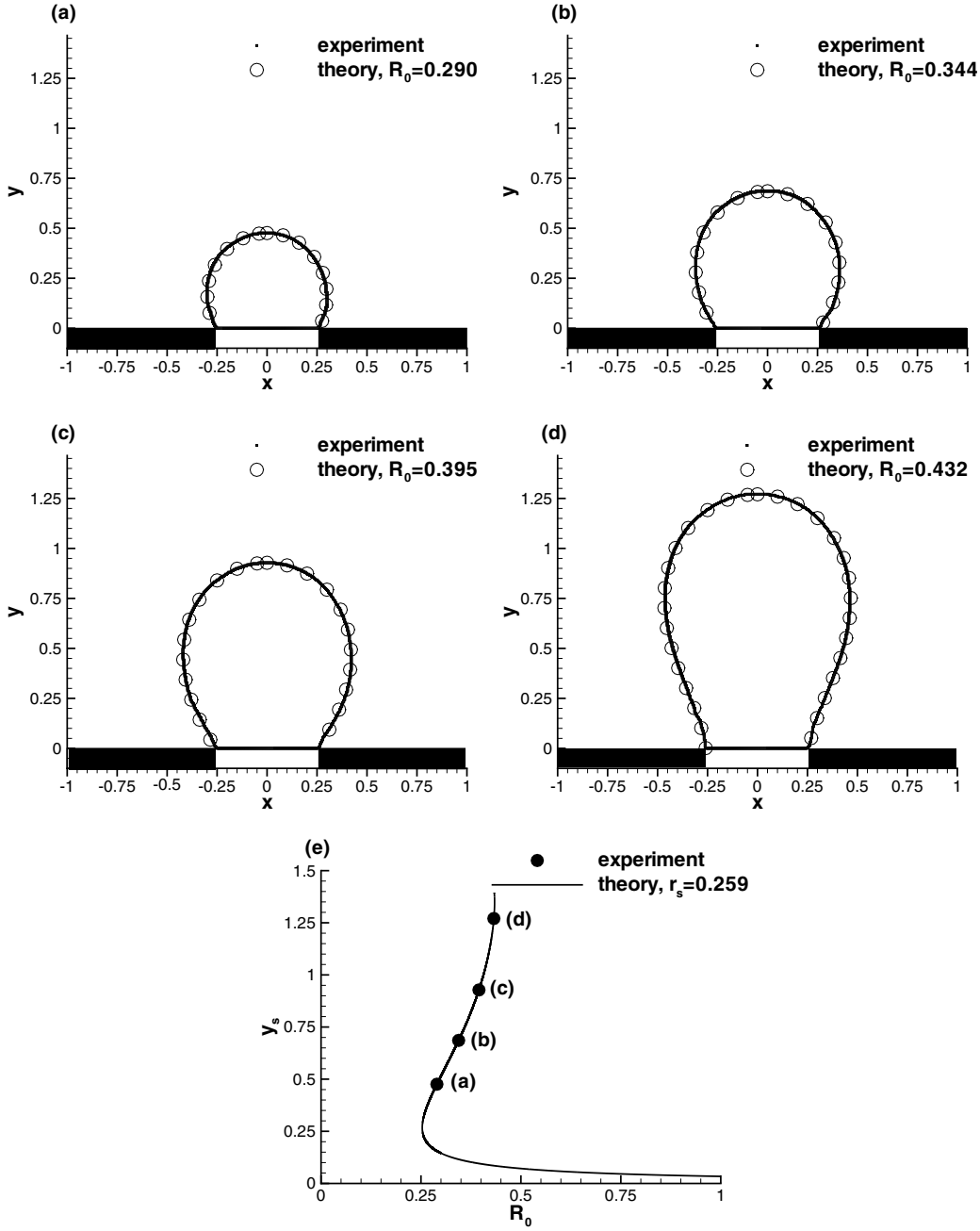

Fig. 5. Comparison between the theoretical solution of static bubble formation with the experimental results using shadow imaging and image processing ((a)–(d)). In (e) the corresponding stages are marked on an R_0–y_s plot. The orifice radius is $r_s = 0.259$.

of computations the bubble base to spread if the instantaneous contact angle of the bubble θ fell below the Young contact angle θ_0. Then the bubble base moved outwards with a constant contact angle and was found to reverse its direction before departure. This means that the model of mode B bubble formation starts also with a horizontal surface ($R_0 \to \infty$, $V = 0$ and $y_s = 0$) and the bubble grows following mode A until θ reaches θ_0. The present calculations were performed with an orifice radius r_s of 0.259 ($\bar{r}_s = 1$ mm). Hence the proposed model for computing the formation of bubbles only switched from mode A to mode B formation if $\theta_0 > \theta_{\min}(r_s = 0.259) = 55.90$ was defined (see Table 1), otherwise the bubble was formed at the rim of the orifice (mode A).

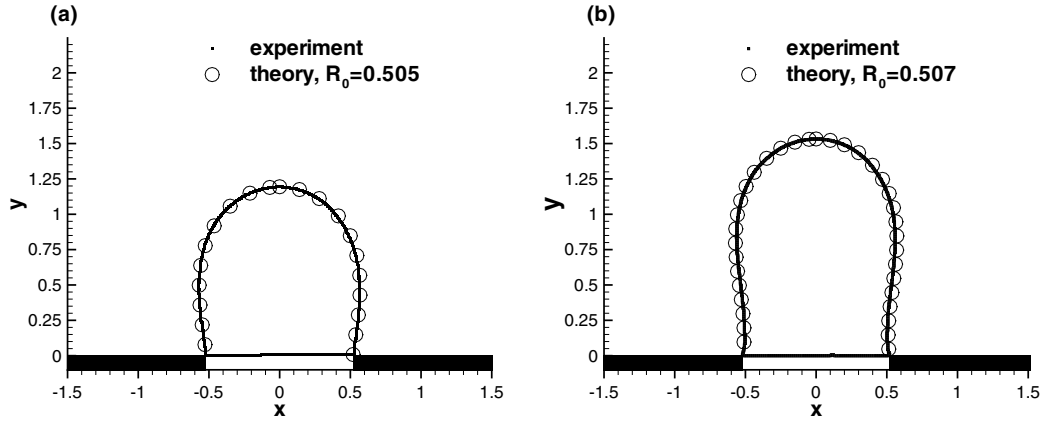

Fig. 6. Comparison between the theoretical solution of static bubble formation with the experimental results using shadow imaging and image processing. The orifice radius is $r_s = 0.518$ ($\bar{r}_s = 2\,\text{mm}$).

Table 1
Summary of the results of mode A bubble formation

r_s	$V_{\max}$	$R_{0,\max}$	$y_{s,\max}$	V_n	$\theta_{\min}$	$y_{s,\exp}$
0.130	0.325	0.375	0.325	0.324	39.26	Mode B
0.2	0.483	0.411	1.285	0.480	48.97	–
0.259	0.618	0.433	1.392	0.609	55.90	1.271
0.3	0.714	0.446	1.456	0.694	60.29	–
0.4	0.961	0.473	1.574	0.890	69.94	–
0.5	1.229	0.495	1.661	1.053	78.54	–
0.518	1.281	0.499	1.673	1.078	80.03	1.532
0.6	1.522	0.515	1.725	1.166	86.38	–
0.7	1.837	0.534	1.774	–	93.67	–

In mode B bubble formation, the radius of the bubble base was denoted r_b.

The results are shown in Figs. 7–10. Depicted are a sequence of contours together with the corresponding points on an R_0–V plot for the case $r_s = 0.259$ and $\theta_0 = 108°$ (Fig. 7), the variation of R_0 (Fig. 8), the base radius r_b (Fig. 9), the height y_s and the non-dimensional pressure difference ΔP_s (Fig. 10) vs the bubble volume V

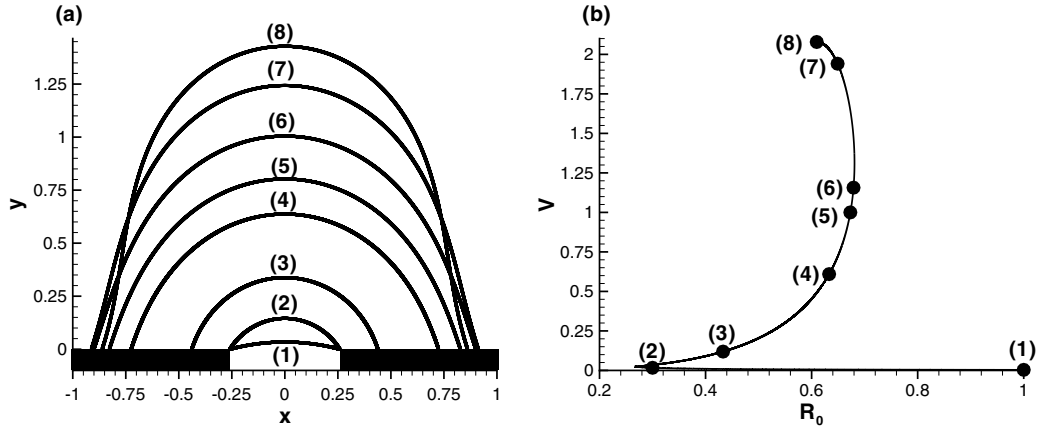

Fig. 7. Theoretical development of the mode B bubble shape (a) and the corresponding locations in the R_0–V plot (b) for the case $r_s = 0.259$ and $\theta_0 = 108°$.

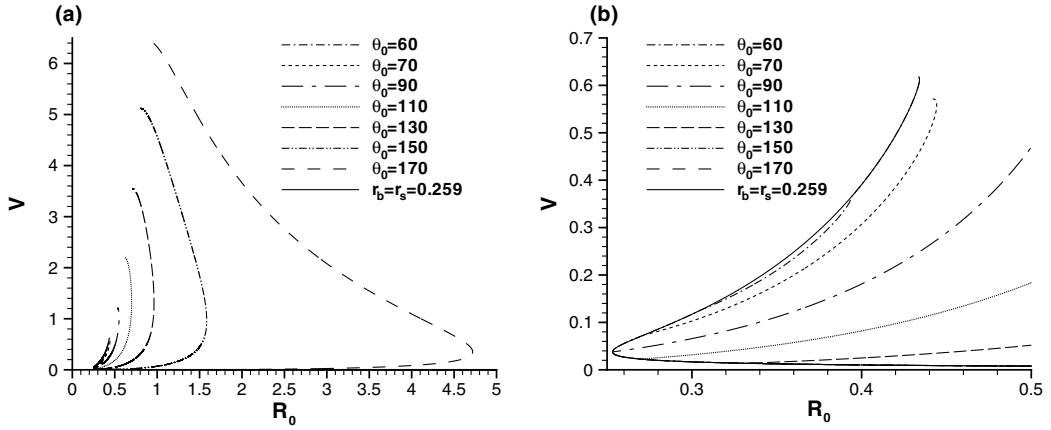

Fig. 8. Influence of the Young contact angle θ_0 on the R_0 distribution (a), (b) shows an enlarged view of (a) in the range $0.25 \leqslant R_0 \leqslant 0.5$. For comparison the case $r_b = r_s = 0.259$ of mode A formation is added.

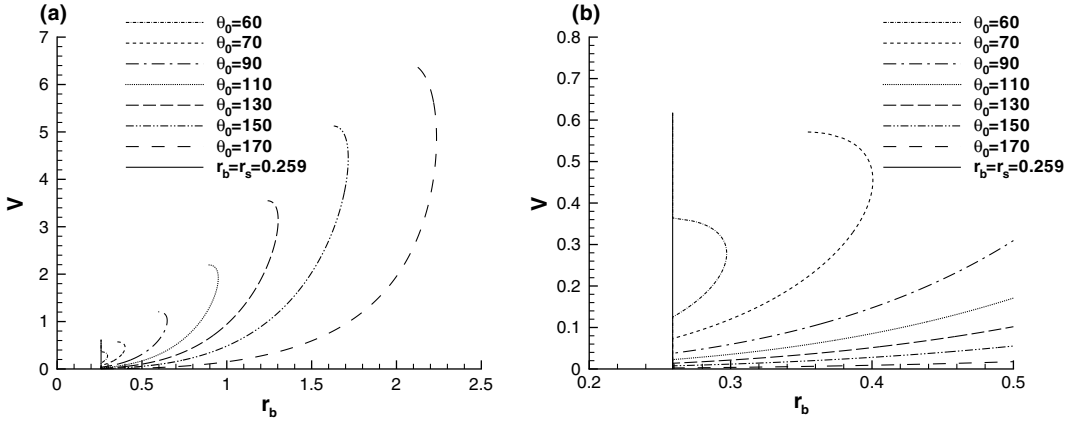

Fig. 9. Variation of the radius of the bubble base r_b for different Young contact angles θ_0 (a), (b) shows an enlarged view of (a) in the range $0.2 \leqslant r_b \leqslant 0.5$. For comparison the case $r_b = r_s = 0.259$ of mode A formation is added.

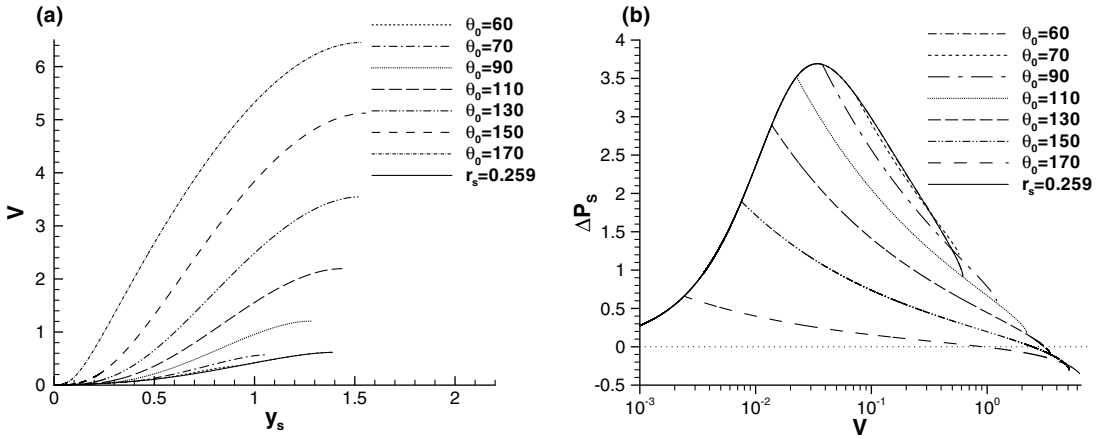

Fig. 10. Bubble height y_s (a) and the non-dimensional pressure difference ΔP_s (b) for different Young contact angles θ_0. For comparison the case $r_b = r_s = 0.259$ of mode A formation is added.

for different Young contact angles. In Figs. 8 and 9 the corresponding case of mode A bubble formation with $r_b = r_s = 0.259$ is added for comparison.

Depending on the Young contact angle, the spreading of the bubble base results in a sharp change of the quantities considered, forming a branch of constant $\theta = \theta_0$. With decreasing θ_0 the mode A distribution is left even later. Stable bubble contours are also found to exist for the case when the bubble base is contracting towards the orifice, before the critical equilibrium is reached and bubble release cannot be avoided (Fig. 9). If the minimum instantaneous contact angle θ_{min} for a given r_s in the mode A regime (see Table 1) is only slightly smaller than θ_0 as defined, one further change in mode can occur due to contraction of the base (Figs. 8(b) and 9(b), case $\theta_0 = 60°$), i.e. the bubble base returns to the orifice rim and obeys the mode A regime (mode A → mode B → mode A).

The results show that with increasing Young contact angle θ_0 the maximal static bubble volume is enhanced significantly. This increase in volume is mostly due to the increase in the base radius (Fig. 9) and to some extent to the bubble height (Fig. 10(a)). The latter can be seen to stay constant for higher values of θ_0. If we consider the influence of varying θ_0 on the non-dimensional pressure difference, it comes out that with increasing θ_0 the maximal pressure decreases. An important feature of this plot is that for large values of θ_0, ΔP_s assumes negative values, i.e. the pressure at the orifice is smaller than the hydrostatic pressure at this height.

If the bubble follows mode B until departure, the values at critical equilibrium depend only on the Young contact angle. The characteristic values of the cases considered here are summarized in Table 2. The maximal volume V_{max} is compared with the data of Fritz [22]. His results are interpolated from tables of Bashforth and Adams [23]. Also given in Table 2 are the maximal base radii $r_{b,max}$ and the radii at the last stable point $r_{b,release}$. As mentioned above, the values in Table 2 are correct also for other orifice radii, if r_s is not too large and quasi-static bubble formation with mode B departure occurs.

The results obtained show clearly the enhanced complexity of the phenomena that occur if mode B formation takes place. Bubbles formed at small orifices are more likely to change to mode B and, hence, can result in huge bubbles compared with mode A: compare, for example, $V_{max} = 0.325$ for the case $r_s = 0.130$ in Table 1 (mode A) with $V_{max} = 2.078$ for the case of a Teflon plate ($\theta_0 = 108°$) in Table 2 (mode B). It can also be seen that the maximum volume and height for the case $\theta_0 = 60°$ (mode A → mode B → mode A) exceeds the value of $\theta_0 = 70°$ (mode A → mode B), which cannot be expected if we look at the tendency of V_{max} with θ_0.

For the experimental investigation of mode B, Teflon plates were used, since Teflon is known to be strongly water-repellent ($\theta_0 = 108°$, [6]). Special care was taken to reduce the roughness of the Teflon plates, since, in contrast to mode A, the influencing parameter on the characteristics is the Young contact angle. Agreement with the predicted results were only possible with the help of nearly smooth Teflon plates. Considered again were the three orifice radii $r_s = 0.130$, 0.259 and 0.518 ($\bar{r}_s = 0.5$, 1 and 2 mm). Also the smallest orifice $r_s = 0.130$ placed on the rough brass plate was found to spread away from the orifice edge (results not shown). Some results are given in Fig. 11 for the case $r_s = 0.518$ and Teflon. The corresponding contour obtained by the theoretical solution was found by fixing the bubble base radius r_b and the height y_s as for mode A. In Fig. 12, the largest experimentally obtained bubble volumes for the three different orifice radii using Teflon are depicted. The differences in the areas included by the contours are smaller than 3.5%. Hence the independence of the

Table 2
Characteristic values of mode B bubble formation for the case $r_s = 0.259$ obtained theoretically

θ_0	V_{max}	$R_{0,max}$	$y_{s,max}$	$r_{b,release}$	$r_{b,max}$	V_{max} [22]
60°	0.618	0.433	1.394	$0.259 = r_s$	0.297	A → B → A
70°	0.571	0.420	1.060	0.352	0.401	0.564
80°	0.849	0.488	1.180	0.466	0.518	0.840
90°	1.206	0.532	1.284	0.595	0.649	1.196
100°	1.653	0.575	1.369	0.739	0.793	1.641
108°	2.078	0.610	1.428	0.862	0.917	–
110°	2.194	0.619	1.439	0.894	0.950	2.185
120°	2.830	0.662	1.496	1.060	1.120	2.832
130°	3.549	0.708	1.529	1.240	1.303	3.536
140°	4.327	0.756	1.547	1.431	1.500	4.303
150°	5.123	0.801	1.555	1.630	1.716	5.084
160°	5.869	0.847	1.546	1.841	1.955	5.855
170°	6.455	0.882	1.535	2.057	2.236	6.463

The maximal volume V_{max} is compared with the data of Fritz [22].

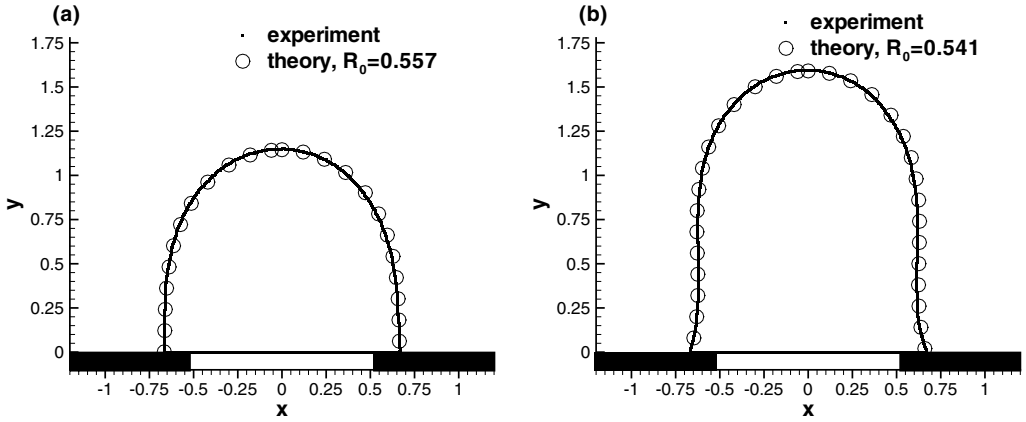

Fig. 11. Comparison of theory and experiment. The orifice radius is $r_s = 0.518$ and the plate material is Teflon.

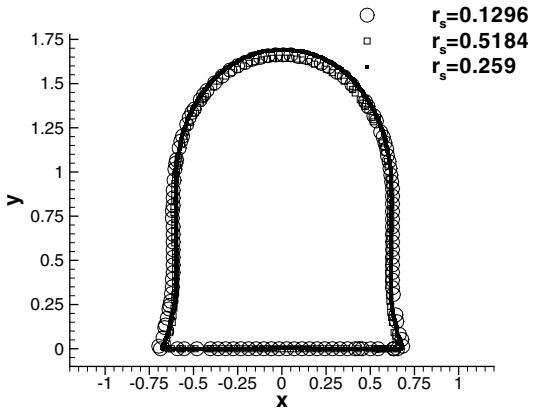

Fig. 12. Maximal bubble contours found for the three orifice radii measured on Teflon. The maximal difference of the area between the three contours is 3.5%.

values at critical equilibrium from the orifice radius is verified as predicted theoretically.

Similarly to Fig. 7(a), some measured contours are depicted in Fig. 13. In both cases the plate material is Teflon theoretically defined by the Young contact angle on a perfectly smooth plate ($\theta_0 = 108°$), whereby the exact value of θ_0 of the three plates is not known. By comparing the two figures, some features can be immediately noticed. In contrast to the theoretical curves the instantaneous contact angle of the measured contours can be seen to be not constant, but smaller than 108°. This results in a bubble shape which is narrower than predicted. Furthermore, the maximal height of the stable bubble stages measured is significantly greater. This behavior can be better understood with the help of Fig. 13(b). Here the two quantities r_b and y_s, which are obtained experimentally from the extracted bubble outline, are plotted from all outlines measured and compared

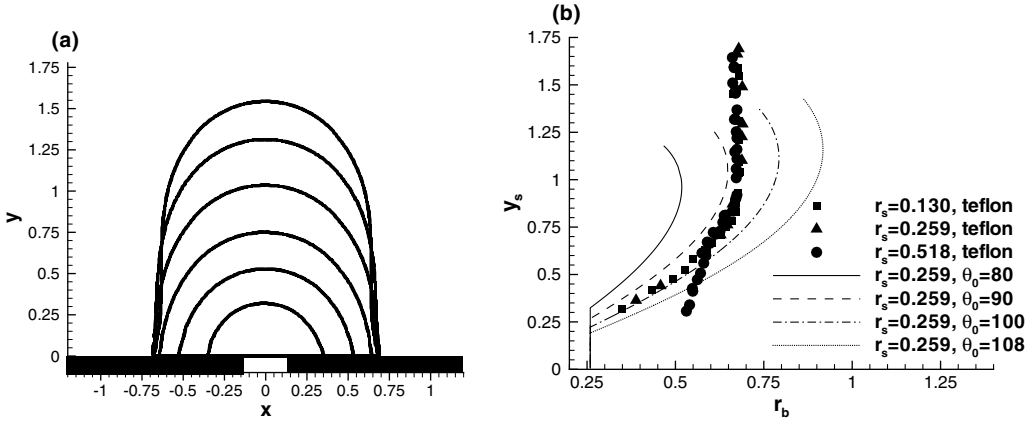

Fig. 13. Some experimental bubble contours for $r_s = 0.130$ measured on Teflon (a) and a comparison of the experimental data with theory by plotting r_b vs y_s (b).

with the theoretical distributions of the cases of constant θ_0 ($r_s = 0.259$). The experimental results for the three orifice radii agree well in the second half of formation. Disagreement exists, as expected, for small values of r_b since initially r_b is related to the orifice radius. Compared with the theoretical distributions, the data points follow the right tendency and are placed between the distributions of $\theta_0 = 90°$ and 100°. At higher values of y_s the radius of the bubble base r_b stays approximately constant and thus crosses other curves of constant θ_0. It should be noted that stable bubble contours are found which are much higher than theoretically predicted near $\theta_0 = 100°$. The results in Fig. 13(b) can be understood in the following way. The bubble base spreads outwards with a constant contact angle, which is smaller than that built under ideal conditions. This is due to the remaining roughness of our Teflon plates, which leads to a decrease in contact angle during outward movement ('receding contact angle', θ_R). On the other hand, an inward movement causes an increase in the instantaneous contact angle ('advancing contact angle', θ_A). This phenomena is called contact angle hysteresis [19]. In our case the model of a receding contact angle describes the lower half of the data points well, e.g. the distribution is parallel to the constant θ_0 lines and lower than $\theta_0 = 108°$ of Teflon. For the second part, where r_b is approximately constant, the bubble base seems to be somehow fixed. Figs. 11(b) and 13(a) indicate that the instantaneous contact angle in the later stages can be seen to be increased, but a significant inward movement cannot be recognized. This is in agreement with the assumption of Dussan [19] that for a given material system an interval between θ_R and θ_A exists where no movement occurs. If we assume the bubble base to be "fixed" at this position, this would explain why the maximal bubble height $y_{s,max}$ shown in Fig. 13(b) is much higher than expected and agrees with $y_{s,max}$ of mode A (Table 1).

5. Conclusions

Bubble formation under quasi-static conditions was investigated theoretically and experimentally. Based on the Laplace equation, predictions are given for two different modes of bubble formation depending on the Young contact angle, which is defined by the solid, gas and liquid employed in the numerical and experimental investigations. In mode A formation, the bubble base remains attached to the orifice rim, whereby the formation of bubbles under spreading of the bubble base is called mode B. The analysis of the results obtained led to the following conclusions:

- The predicted bubble shapes compare extremely well with the experimental counterpart for both modes of formation.
- The characteristics of complete static formation processes were obtained for the two modes theoretically, by arranging families of bubble profiles, for example, for a given orifice radius with increasing volume and height for mode A.
- Mode A formation was found to depend only on the non-dimensional orifice radius ($r_s = \bar{r}_s/a$ with the Laplace constant $a = \sqrt{2\sigma/(g(\rho_l - \rho_g))}$). The characteristics at critical equilibrium, i.e. at the last stable state, at which the bubble volume has its maximum, agree well with the experiments. The characteristics considered were the bubble volume, height, the radius of curvature at the apex, the instantaneous contact angle at the bubble base and the non-dimensional pressure difference at the orifice mouth.
- The transition from mode A to mode B bubble formation is dictated by the Young contact angle. Transition occurs if the instantaneous contact angle at the bubble base falls below the Young contact angle. Small orifice radii favor spreading of the bubble base, since smaller values of the instantaneous contact angle are reached during the formation process. For mode B formation, the bubble was found to contract towards the orifice before detachment. Hence sequences including two transitions ($A \rightarrow B \rightarrow A$) are also described.
- In addition to the fluid properties, the Young contact angle defines the maximum stable size of the mode B bubble. A non-wetting plate material (Teflon) was used for the experiments of mode B formation. The experimental results agree with the predictions in general. Disagreement due to the surface roughness of the plate is explained by means of an observed contact angle hysteresis.
- The plate material was shown to have a strong influence of the characteristics of the formation process. For instance, large differences in bubble volume at detachment were found between modes A and B formation for a constant orifice radius.

Acknowledgment

One of the authors (D.G.) gratefully acknowledge the support received from the Bayerische Forschungsstiftung, Germany.

References

[1] W. Siemens, Gasblasen in Flüssigkeiten, Teil I: Entstehung von Gasblasen an nach oben gerichteten kreisförmigen Düsen, Chem. Ingen. Tech. 26 (1954) 479–496.
[2] V. Carey, Liquid–Vapor Phase-Change Phenomena, Taylor and Francis, Washington, DC, 1992.

[3] F. Durst, H. Beer, Blasenbildung an Düsen bei Gasdispersion in Flüssigkeiten, Chem. Ingen. Tech. 18 (1969) 1000–1006.
[4] M. Longuet-Higgins, B. Kerman, K. Lunde, The release of air bubbles from an underwater nozzle, J. Fluid Mech. 230 (1991) 365–390.
[5] R. Clift, J. Grace, M. Weber, Bubbles, Drops, and Particles, Academic Press, New York, 1978.
[6] J. Davies, E. Rideal, Interfacial Phenomena, second ed., Academic Press, New York, 1963.
[7] J. Gibbs, Scientific Papers (Dover Reprint, New York, 1961) 1, 1906, p. 326.
[8] D. Dyson, Contact line stability at edges: comments on Gibbs's inequalities, Phys. Fluids 31 (2) (1988) 229–232.
[9] J. Oliver, C. Huh, S. Mason, Resistance to spreading of liquids by sharp edges, J. Colloid Interface Sci. 59 (3) (1977) 568–581.
[10] E. Bayramli, S. Mason, Liquid spreading: edge effect for zero contact angle, J. Colloid Interface Sci. 66 (1) (1978) 200–202.
[11] A. Chesters, Modes of bubble growth in the slow-formation regime of nucleate pool boiling, Int. J. Multiphase Flow 4 (1978) 279–302.
[12] A. Chesters, An analytical solution for the profile and volume of a small drop or bubble symmetrical about a vertical axis, J. Fluid Mech. 81 (1977) 609–624.
[13] J. Paddy, A. Pitts, The stability of axisymmetric menisci, Philos. Trans. A Roy. Soc. 3 (1973) 489–528.
[14] E. Pitts, The stability of pendent liquid drops. Part 2. Axial symmetry, J. Fluid Mech. 63 (1974) 487–508.
[15] E. Pitts, The stability of a drop hanging from a tube, J. Inst. Math. Appl. 17 (1976) 387–397.
[16] E. Shoukry, M. Hafez, S. Hartland, Separation of drops from wetted surfaces, J. Colloid Interface Sci. 53 (2) (1975) 261–270.
[17] A. Kovitz, Static fluid interfaces external to a right circular cylinder—experiment and theory, J. Colloid Interface Sci. 50 (1) (1975) 125–142.
[18] S. Gnyloskurenko, A. Byakova, O. Raychenko, T. Nakamura, Influence of wetting conditions on bubble formation at orifice in an inviscid liquid. Transformation of bubble shape and size, Colloids Surf. A 218 (2003) 73–87.
[19] V.E. Dussan, On the spreading of liquids and solid surfaces: static and dynamic contact lines, Ann. Rev. Fluid Mech. 11 (1979) 371–400.
[20] T. Lohnstein, Theorie des Abtropfens, Ann. Phys. 4 (1906) 237–267.
[21] K. Lunde, R. Perkins, A method for the detailed study of bubble motion and deformation, in: A. Serizawa, T. Fukano, J. Bataille (Eds.), Advances in Multiphase Flow, Elsevier Science Publisher, Amsterdam, 1995, pp. 395–405.
[22] W. Fritz, Berechnung des Maximalvolumens von Dampfblasen, Phys. Zeits. 36 (1935) 379–384.
[23] F. Bashforth, J. Adams, An Attempt to Test the Theories of Capillary Action, Cambridge University Press, Cambridge, 1883.